Key Points:
- The dynamic fragmentation and lubrication mechanisms of coseismic landslides have been analyzed by discrete element method
- The landslide is triggered by the seismic shaking-induced rock fragmentation and reduction of basal stress ratio
- The widespread slope fragmentation and lubrication are the intrinsic features of landslide irrespective of its triggering mechanism

Supporting Information:
- Supporting Information S1
- Data Set S1
- Movie S1

Correspondence to:
T. Zhao,
zhaotao@scu.edu.cn

On the Dynamic Fragmentation and Lubrication of Coseismic Landslides

Tao Zhao[1,2] [iD] and Giovanni Battista Crosta[3] [iD]

[1]State Key Laboratory of Hydraulics and Mountain River Engineering, College of Water Resource and Hydropower, Sichuan University, Chengdu, China, [2]Department of Civil and Environmental Engineering, Brunel University London, London, UK, [3]Department of Earth and Environmental Sciences, Università degli Studi di Milano Bicocca, Milan, Italy

Abstract The three-dimensional discrete element method has been employed to analyze the dynamic fragmentation and lubrication mechanisms of coseismic Tangjiashan landslide induced by the 2008 Ms 8.0 Wenchuan earthquake. The numerical results show that the internal rock damage occurs and propagates gradually along the basal failure plane due to seismic shaking. At the peak seismic shaking, a sudden increase of tensile and shear stresses can lead to the complete breakage of basal bonds. This is associated with a sudden relief of overburden stress and rapid decrease of basal stress ratio. Thus, the slope fails as a whole and moves quickly downslope. In this process, several large transversal cracks develop at the middle and upper rear regions, disintegrating the slope mass into several large blocks. During landslide propagation, the thickness of basal fragmented layer increases progressively due to intense shearing, and the basal stress ratio reduces accordingly from 0.68 to 0.28. The reduction of landslide basal stress ratio occurs when the strong basal resistance is overcome by seismic- and gravity-induced shear forces together with intense particle rearrangements. It can be quantified by vibrational and rotational granular temperatures of the basal shear layer, with the peak values of 35.2 and 11.6 m^2/s^2, respectively. The widespread internal slope fragmentation and subsequent lubrication have been identified as the key mechanisms governing landslide motion, which appear to be the intrinsic features of landslide irrespective of its triggering mechanism. The seismic shaking is more relevant to the detachment than to the spreading of landslide mass.

1. Introduction

Coseismic landslides can be catastrophic, as they are always associated with almost instantaneous slope collapse and spreading, posing significant hazards to human lives and lifeline facilities worldwide. These events have been widely observed close to the main earthquake fault zone and on the hanging-wall side (Huang & Li, 2009). In addition, landslides occurring near the deeply incised river valleys with steep bank slopes could potentially create landslide dams blocking the river channel (Crosta et al., 2011; Evans et al., 2011; Xu et al., 2013; Zhao et al., 2017b). The subsequent breaching of landslide dams may lead to serious downstream flooding and inundation, often with large social and economic consequences (Wu et al., 2014). These hazards are still under vigorous research due to their significant destructive power as well as the still unexplained initiation and propagation mechanisms of slope failure (Legros, 2002).

For many years, efforts have been devoted to study the failure of slopes and the subsequent runout (Bowman & Take, 2015; Bowman et al., 2012; Cascini et al., 2014; Evans et al., 2009; Huang & Yuin, 2010). However, less attention has been paid to analyzing the mechanism of coseismic landslides with complex geological and topographical settings (Jibson & Harp, 2016; Katz et al., 2014; Meunier et al., 2007). In initiating landslide, the earthquake loading plays a pivotal role by supplying an additional kinetic energy for slope destabilization (Hori et al., 2013; Kokusho & Ishizawa, 2007). As a result, the mountain slopes can be shattered and collapse at high speed during seismic shakings (Huang et al., 2012). In addition, the ground shaking can also loosen and weaken the slope materials, creating open holes and cracks for water infiltration into the slope body (Palmer, 2017). These conditions are crucial for subsequent catastrophic landslides occurring on the upper part of a mountain slope, where strong unloading and weathering effects are apparent. By investigating landslides developed after the Wenchuan earthquake, Tang et al. (2011) concluded that the seismic shaking and subsequent strong rainfalls severely disturbed the loose debris materials on mountain slopes, prompting the reactivation of some preexisting landslides as well as the generation of new ones.

According to field observations, the density of the mapped landslide concentration is normally associated with the seismic shaking magnitude (Chigira et al., 2010). The spatial distribution of landslides shows an evident concentration in areas with horizontal seismic acceleration component larger than 0.8 g (g: the gravitational acceleration; Dai et al., 2011; Khazai & Sitar, 2004; Tang et al., 2011). These areas are located mainly on the hanging-wall sides of the major seismic faults and steep river valleys (Huang & Li, 2009; Tang et al., 2011). Yin et al. (2009) stated that the vertical component of seismic shaking also has a great influence on the initiation of landslides, in terms of slope fracturing, ejection, and fragmentation. The corresponding failure plane of landslides can be classified into three types as concave, convex, and terraced. Fukuoka et al. (2004) reported that even very gentle slopes can fail and travel long distances under strong seismic-induced ground shaking. In these events, the solid materials are highly liquefiable, increasing the slope mobility significantly. Kokusho and Ishizawa (2007) proposed an energy-based slope failure evaluation method to analyze the slope deformation and subsequent landslide runout. They stated that even under an extremely strong earthquake, the highly mobile slope failures can only occur when the friction angle reduces to a value near or smaller than the slope inclination angle. This conclusion was supported by some well-devised shaking table tests of dry sand slopes. They also suggested that the energy input by earthquake is far smaller than the potential energy required to trigger highly mobilized landslides/rockslides.

In addition, the apparent friction coefficient (defined as the ratio of landslide fall height, H, to spreading distance, L) decreases with the increasing slope volume; that is, large landslides can always exhibit longer spreading distances (Campbell et al., 1995; Crosta et al., 2017; De Blasio & Elverhøi, 2008; Legros, 2002). Based on a series of 2-D discrete element analyses, Campbell et al. (1995) and Johnson and Campbell (2017) proposed that the whole slope mass can be completely sheared during sliding and the apparent friction coefficient of landslide increases with the shear rate. As large landslides always experience very low shear rates due to the large thickness, they manifest relatively low frictional resistance. However, limitations also exist, as these studies only considered a very simple model configuration of completely fragmented slope materials at the start of landslide simulations. As a result, an insightful study on the progressive fragmentation of slope mass and increase of shear zone thickness was not possible. From a series of discrete element simulations, Johnson et al. (2016) deduced that long runout landslides occur preferentially when the normal stress along the sliding plane is relieved due to pressure variations. This phenomenon can reasonably support the hypothesis of landslide acoustic fluidization (Melosh, 1979). The corresponding wavelength of acoustic vibration for long runout landslide can be effectively determined by the size of rock fragments in the slide.

Since the slope motion and deformation are closely related to the seismic shaking, it is necessary to analyze the initiation and propagation mechanisms of coseismic landslides. In this regard, the current research has focused on modeling the progressive slope failure under seismic loading via discrete element method (DEM; Cundall & Strack, 1979), aiming to provide new insights into the detailed microresponses and macroresponses of coseismic landslides. This paper is organized as follows: In section 2, the background of the Tangjiashan landslide is given. Then, the DEM model configuration of a layered slope structure and seismic loading conditions is illustrated in section 3. In section 4, some preliminary numerical results of the Tangjiashan landslide modeling are provided. The capability of the DEM in analyzing the coseismic landslide and possible mechanisms of landslide friction reduction are discussed and summarized in the last two sections.

2. Background of the Tangjiashan Landslide

The 2008 Ms 8.0 Wenchuan earthquake has triggered more than 60,000 catastrophic landslides, rockfalls, and debris flows along the Longmenshan seismic fault zone within a 300-km-long and 10-km-wide region (Fan et al., 2012; Gorum et al., 2011; Huang & Fan, 2013; Huang et al., 2012). The induced landslides are commonly discontinuous and characterized by very gentle sliding surfaces, which caused a great number of casualties, loss of properties, and also significant changes of geo- and bio-environments. Among these landslides, the Tangjiashan landslide is one of the largest and most dangerous one because the debris deposits formed a giant landslide dam (~800 m long, 611 m wide, and 82 to 124 m high, with volume of approximately 2.04×10^7 m^3) in the upstream section of the Jian River (Xu et al., 2009). This landslide occurred during the major seismic shaking, and it moved atop of the fragmented bedrock, scouring the bank of Jian River for nearly 2,400 m (Yin et al., 2009; see Figure 1). As the landslide occurred within a very short time period, the failed slope mass went through mainly translational and partially rotational movements along the failure
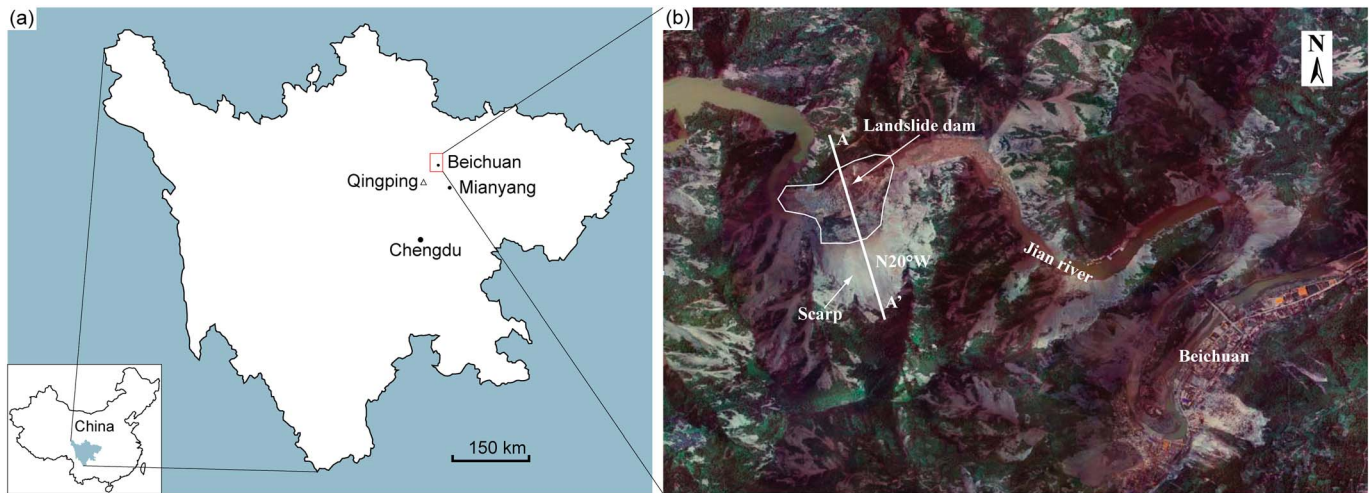
Figure 1. (a) Map of Sichuan province and the location of Tangjiashan landslide; (b) aerial view of the Tangjiashan landslide dam (A-A' is the cross section studied in this paper). △ in (a) is the Qingping seismic station.

plane. The landslide dam, as described by Xu et al. (2009), in a first approximation, consists of mainly three layers of grayish black siltstone of the Qingping Formation of Cambrian age, with a slight increase in grain size with depth. They can be identified as the heavily fragmented rocks with soil in the top layer, the boulders and blocks in the middle layer, and the nondisintegrated rock masses in the bottom layer. The estimated initial slope profile, layered stratigraphic structure, and the final deposit characteristics are illustrated in Figure 2, with a slope inclination angle (θ_s) of 45°.

Chang and Zhang (2010) examined the particle size distribution (PSD) of the Tangjiashan landslide dam at different depths. As shown in Figure 3, a large amount of fine materials was found at the surface of landslide dam, with grain size ranging from 0.001 to 50 mm. The medium-sized debris materials were located in the region of depth 10 to 40 m, with grain size ranging from 0.01 to 200 mm. The large particles and blocks were found at depth beyond 40 m with grain size ranging widely from 1 to 1,500 mm. This is a peculiar deposition pattern with respect to commonly observed rockslide-avalanches, but it could result from the limited runout with respect to other more mobile rock avalanches. Unfortunately, the seismic accelerations were not recorded at the Beichuan seismic station, due to the equipment failure. The nearest seismic station in Qingping county is 46 km away (see Figure 1). Thus, the seismic acceleration records at this station are used
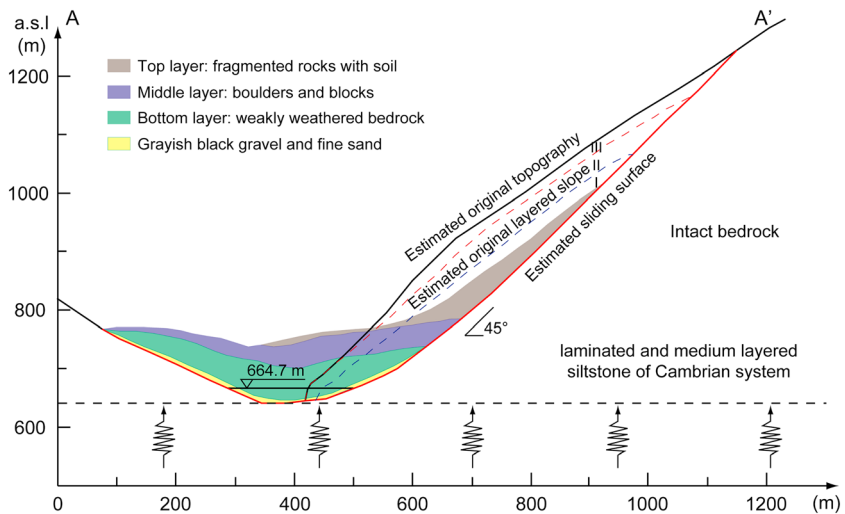

Figure 2. Cross section of the Tangjiashan landslide and landslide dam. The layered lithologic structure is estimated according to Xu et al. (2009). The seismic excitations are assumed to be applied at the bottom bedrock along a horizontal dashed line in the DEM simulations. a.s.l = above the sea level.
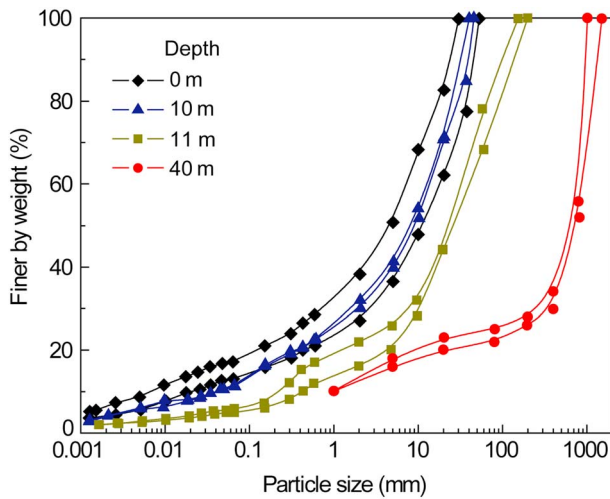
Figure 3. Particle size distribution of the Tangjiashan landslide dam at different depths below the deposit surface (data from Chang and Zhang, 2010).

as the representative seismic loading wave data for analyzing the Tangjiashan landslide. According to the recorded ground accelerations, the ground velocity and displacement have been obtained by integrations, baseline corrections, and band-pass filtering (Butterworth type, with cutoff frequency in the range of [0.2, 20] Hz; Chang & Taboada, 2009) via the software SeismoSignal (Seismosoft, 2017), as shown in Figure 4. The recorded seismic wave data show that the strong seismic shaking occurred at 15–30 s after the record starting time (20 s after the earthquake initiation). The calculated ground displacements are employed in the discrete element simulations as base excitations.

3. DEM Model Configurations

In the current study, the open-source DEM code ESyS-Particle (Abe et al., 2004; Zhao et al., 2015) has been employed to run simulations presented herein. The basic DEM theory and rigorous calibrations can be found in Zhao et al. (2017a) and will not be repeated herein. In short, the brittle rock mass is simulated as an assembly of particles cemented together via the so-called parallel bond model (Jiang et al., 2015; Potyondy & Cundall, 2004). The motion of each single particle is governed by the Newton's second law of motion, and the contacts between particles can be calculated by the well-defined linear elastic spring-dashpot model. The input parameters of the DEM model are listed in Table 1.

In the parallel bond model, a 3-D formulation of bond breakage constitutive law has been employed to determine whether an interparticle bond breaks, as

$$\frac{|F_{bn}|}{F_{bnMax}} + \frac{|F_{bs}|}{F_{bsMax}} + \frac{|M_b|}{M_{bMax}} + \frac{|M_t|}{M_{tMax}} \geq 1, \tag{1}$$

where F_{bn} and F_{bs} are the normal and shear bonding forces; M_b and M_t are the bending and twisting torques; and F_{bnMax}, F_{bsMax}, M_{bMax}, and M_{tMax} are the threshold values of normal, shear, bending, and twisting bonding strengths of a specific bond, respectively.

According to the layered lithologic structure of the final landslide deposit reported in Xu et al. (2009), the initial slope mass is assumed to be composed of three layers aligning approximately parallel to the slope failure plane in the DEM model (see Figure 2, layers I, II, and III). To generate the slope model by DEM, Zhao et al. (2016) has proposed a simple and efficient *hopper discharge technique*, by which the spherical particles are allowed to fill up a slope domain of complex geometry. This method has been adopted in the current study for generating the three-layer structure of Tangjiashan slope. The DEM simulations employ the plane strain boundary condition in which the out-of-plane model is 20 m wide and confined by free slip rigid boundary walls. In this framework, a number of spherical particles are used to fill up this unit slope domain, which can be regarded as one fraction of the real Tangjiashan slope. Ideally, the PSD used in the numerical model should match the PSD curves in Figure 3. However, the use of very fine particles in discrete element simulations would lead to extremely high computational cost by an enormous number of particles generated in the numerical model and very small iteration time steps. To overcome this numerical limitation, the particle sizes used in the DEM model have been tuned to fit the model configuration, reaching a good level of representativeness and at the same time optimizing the computational effort. Thus, the particle radii of three different slope layers (i.e., from the bottom up, layers I, II, and III) are set uniformly within the ranges of [1,500, 2,000], [1,000, 1,500], and [800, 1,000] mm, respectively. The number of particles in each layer is 15,787, 34,911, and 46,712 respectively. The granular assembly is bonded together with assigned bonding strength (*c*) and Young's modulus (E_b) to form the initially intact slope. For these large particles with sizes comparable to real rock mass blocks (~1.6–4 m), the interparticle cementation (i.e., bonds in DEM) could effectively represent the rock bridges between adjacent blocks/particles, contributing some cohesion to the rock mass. The landslide failure plane is represented by a collection of triangular meshes, onto which a layer of uniformly graded grains (*r* = 1,500–2,000 mm) is glued to mimic a nonerodible and rough base (Jing et al., 2016; Utili et al., 2015).
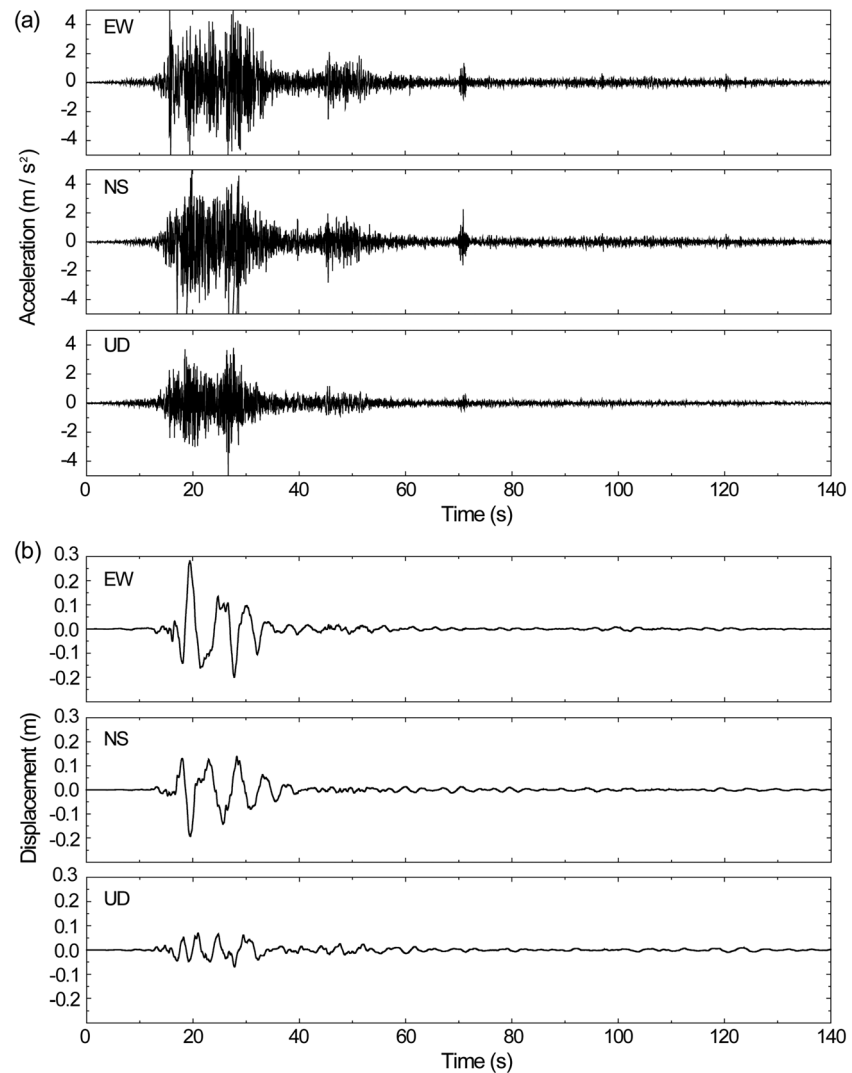
Figure 4. Seismic wave records from the Qingping Station (after the baseline correction; see Figure 1 for location). (a) The ground accelerations in EW, NS, and UD directions; (b) the calculated ground displacements in EW, NS, and UD directions. Data are provided by the China Strong Motion Network Center (http://data.earthquake.cn/index.html). The record starts at 14:28:24, GMT +8, 12 May 2008.

Table 1
Input Parameters of Coseismic Landslide Modeling by DEM

DEM parameters	Value	DEM parameters		Value
Particle radius, r (m)	0.8–2	Bonding strength, c (MPa)	Layer I	10
Particle density, ρ (kg/m³)	2,650		Layer II	5
Particle Young's modulus, E (GPa)	5		Layer III	3.3
Particle Poisson ratio, υ	0.25	Bonding Young's modulus, E_b (GPa)	Layer I	3
Particle viscous damping coefficient, β_1	0.01		Layer II	1.5
Basal viscous damping coefficient, β_2	0.05		Layer III	1
Particle friction angle, θ_1 (degree)	30	Gravitational acceleration, g (m/s²)		9.81
Basal slope friction angle, θ_2 (degree)	30	DEM time step, Δt (s)		10^{-4}

Note. DEM = discrete element method.

Due to the lack of detailed information of material properties, practical estimations of rock strength and bulk Young's modulus have been performed for the studied slope (mainly sandstone) based on the suggested values in Goodman (1989) and Hoek and Brown (1997), as shown in Table 1. In particular, the particle Young's modulus and Poisson's ratio are 5 GPa and 0.25, respectively. According to the field observations, the slope consists of mainly weathered sandstones, and their weathering intensity decreases with depth (Xu et al., 2009). Thus, in the current analyses, we have assigned the rock mass properties (e.g., bonding strength and Young's modulus) increasing with depth from the surface (layer III) to the inner rock mass (layers II and I; see Table 1). In fact, the bonding cohesion between rock blocks can vary widely depending on the slope weathering intensity. Here the bonding cohesion is firstly set as 10 MPa to particles in layer I for a preliminary investigation, while a systematic parametric study on this parameter will be given in section 4.5. In addition, the viscous damping force (proportional to the relative velocity of particles in contact) has been employed at contacts to replicate the energy dissipation by particle asperities being sheared off and the plastic deformations of the contacting particles occurring in the vicinity of the contact points. The damping coefficient of granular particles within the rock mass is 0.01, and 0.05 for particles along the failure plane. The high viscous damping at the base could effectively mimic the absorbing boundary condition for the seismic wave transmission and reflection at the slope base (McNamara, 2013).

In numerical simulations, the seismic-induced ground displacements are applied along the base of the model (see the horizontal dashed line in Figure 2). It is worth noting that the landslide profile direction is N20°W (see Figure 1), which should be considered for calculating the resultant seismic shaking in the slide direction starting from the EW and NS seismic components. The vertical displacement is set as the UD component of seismic motion, while the lateral seismic shaking of the numerical model is ignored due to the imposed plane strain boundary condition. In addition, the slope shaking is not synchronized along the failure plane due to different elevations. In the analyses, the seismic wave is assumed to travel from the bedrock upwards into the slope mass. The nodes of the predefined failure plane mesh start to move only when the seismic shaking wave reaches their elevation. As stated by Li et al. (2011), relatively low P wave velocities near the ground surface were found in this area of the Longmenshan fault range consisting of mainly Quaternary deposits (Wu et al., 2009). Thus, the traveling velocity of P wave in this region is estimated as 2,000 m/s (v_p). For simplicity, we assume that the slope mass consists of an assembly of elastic and isotropic rigid particles, such that the seismic waves can propagate at a constant velocity, v_p, within the bedrock and the slope. In this study, all numerical simulations were run on standard desktop computers (Intel® Core™ i7 CPU, 4.00 GHz × 8, and 16 GB RAM) for a total of around 112 hr in each run.

4. Results of Tangjiashan Landslide Modeling

4.1. Dynamics of Landslide Motion

Using the DEM model, simulations of the coseismic Tangjiashan landslide have been performed, as shown in Figure 5 (also see the animation in the supporting information). According to the figure, the slope failure occurs at about 16 s since seismic shaking record begins when a transversal tension crack occurs at the upper rear section of the slope (see the tail crack in Figure 5b). In the meantime, the ground seismic shaking accelerations in three directions all approach very large values (see Figure 4). After failure, the bulk slope mass moves as a whole along the sliding plane. From 16 to 20 s, there is an abrupt change of ground motion (see the seismic acceleration vectors and the EW and UD displacement components in Figure 4b), such that high shear stresses would localize at the base. As a result, cracks develop and grow to completion quickly along the basal failure plane, which facilitate the subsequent downslope acceleration of landslide. During the sliding process, the solid materials are translated and partially rotated along the failure plane, as shown in snapshots at successive time steps. At the early stage (e.g., Figure 5c at 17 s), some cracks occur in the tail region of the slope due to strong downward pulling forces (tensile stresses) exerted by the lower slope mass. The detached fragments in layer III are partially incorporated into and bulldoze the moving substrate layer II, creating several ridges in the final deposit (see blue arrows in Figures 5f–5i). In the valley bottom, the slope inclination changes at several locations, such that the tensile stress would increase suddenly when the slope mass moves across these areas. The resultant fragmented portions can be observed clearly on Figures 5f–5i (the regions delimited by red dashed curves) within the moving slope mass (see also the internal transversal damage zones in Figure 9). The bottom layer is wrapped by the middle layer in the frontal region, resulting in a relatively short spreading distance. The granular deposit profile changes little after 50 s, and only few
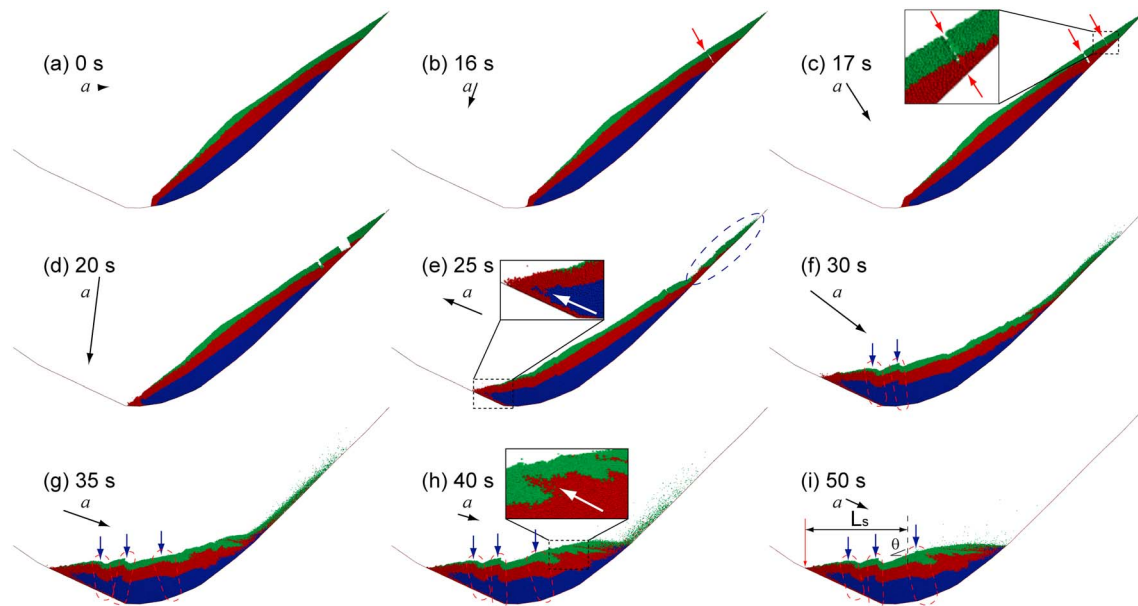
Figure 5. Snapshots of Tangjiashan landslide modeling at time (a) 0 s, (b) 16 s, (c) 17s, (d) 20 s, (e) 25 s, (f) 30 s, (g) 35 s, (h) 40 s and (i) 50 s. The inset plot in (c) shows the details of cracks developed at the landslide initiation stage. The ground seismic acceleration is plotted as a vector on each snapshot. In (i), the runout distance and deposit inclination angle of the landslide are labeled as L_s and θ, respectively. L_s is measured from the initial slope toe to the final deposit front. The red arrows point to the major cracks; the white arrows indicate the internal layer intrusion direction; the blue arrows and dashed red ellipses delimit the large slope decollement zones; the blue dashed ellipse in (e) delimits the detached slope tails.

surface clasts continue moving near the tail surface. The total landslide duration time (50 s) matches that reported in Xu et al. (2009) for the real Tangjiashan landslide. The final runout distance (L_s in Figure 5i) measured in the numerical simulation is 310 m, which is slightly shorter than that reported in Xu et al. (2009), 344 m. In addition, the inclination angle of final debris deposit ($\theta \approx 22°$) is slightly larger than the real one (20.5°, measured in the middle of the deposit, in Xu et al., 2009). The gross stratigraphic relations are preserved during the emplacement apart from the frontal region where a reversal is partially observed for the occurrence of a sort of recirculating movement of the fragmented particles from the upper layer toward the front and below it (see the inset plot in Figure 5e). The motion and the recycling below the front can also be partially controlled by the local geometry at the valley bottom. This phenomenon of stratigraphy preservation has also been reported in some well-documented numerical and field examples (Campbell et al., 1995; Strom, 1999).

The evolution of landslide propagation velocity has been analyzed in terms of the mean velocities of the whole slope mass and the landslide frontal region, as shown in Figures 6a and 6b. Here the landslide frontal region is defined as the slope toe of width 2.5 m along the sliding direction, which consists of 54 particles. According to Figure 6a, it can be seen that before failure, the mean slope velocity fluctuates slightly, as controlled by the ground seismic motion (see Figure 4). The slope fails at 14 s (t_0), and it starts to move downslope. From 14 to 25 s, both the vertical and horizontal velocity components increase approximately linearly with time, reaching the peak values of 13 and 20 m/s, respectively, after a short period of time (at 23.2 s for v_{v_s} and 26.5 s for v_{h_s}). These peak velocities occur when the slope mass reaches the bottom and starts to collide onto the opposite bank of the valley. During this period of time, the ground shakes intensely, especially in the vertical directions. The subsequent landslide deposition leads to gradual decrease of v_{v_s} and v_{h_s}, and they finally become zero after 50 s. Figure 6b shows that the velocity components of the sliding front fluctuate intensely during the landslide propagation and deposition. After t_0, as the landslide moves toward the bottom and subsequently moves upward onto the other bank, the vertical velocity component (v_{v_f}) firstly increases slightly to the positive peak value of 3.8 m/s at 18.3 s and then decreases quickly to the negative peak value of −5.85 m/s at 24.1 s. Here the negative vertical velocity indicates that the landslide frontal region moves upwards. When $v_{v\_f} = 0$ m/s at around 20.1 s, the horizontal velocity component of the landslide front (v_{h_f}) reaches the peak value of 16.5 m/s. The subsequent landslide motion and collisions
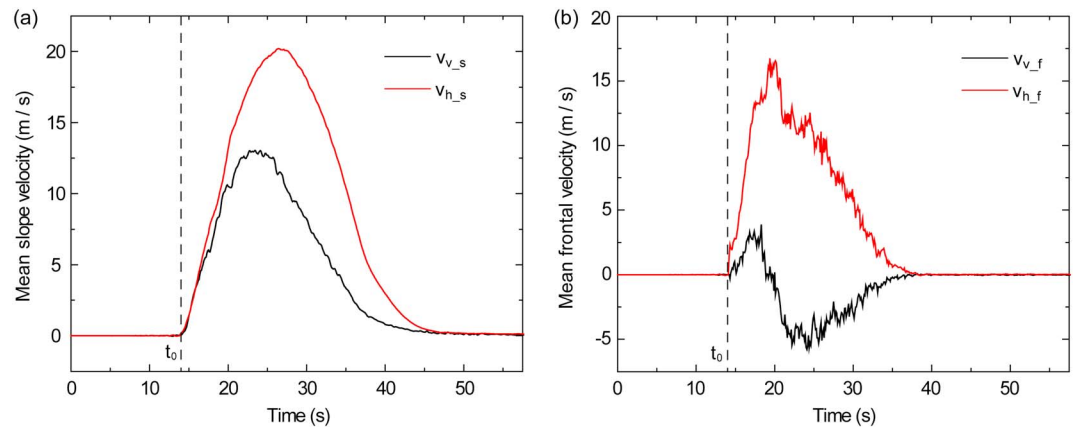
Figure 6. Evolution of landslide propagation velocity. (a) The vertical (v_{v_s}) and horizontal (v_{h_s}) velocity components of the whole slope mass; (b) the vertical (v_{v_f}) and horizontal (v_{h_f}) velocity components of the landslide frontal region. The velocity components along the sliding direction (A′-A) and vertically downward are denoted positive. t_0 denotes the time of slope failure.

cause several apparent fluctuations of slope frontal velocities, which might result from the influence of intense slope-ground interactions, together with the ground seismic shaking.

4.2. Evolution of Slope Force Chains

The evolution of slope internal structure can be illustrated by a series of force chains plotted as a network of straight lines connecting the particle centers, with the thickness proportional to the magnitude of particle interaction forces (e.g., the normal and tangential interparticle contacting and bonding forces). The distribution of force chains reflects the magnitude and orientation of major principal stresses. In the analyses, different types of interaction forces have been plotted in distinctive colors, as shown in Figure 7 (the normal compression and tension bonding forces are colored blue and red; the normal and shear contact forces are in black and green, respectively). To better present the results, some blue dashed lines are used to show
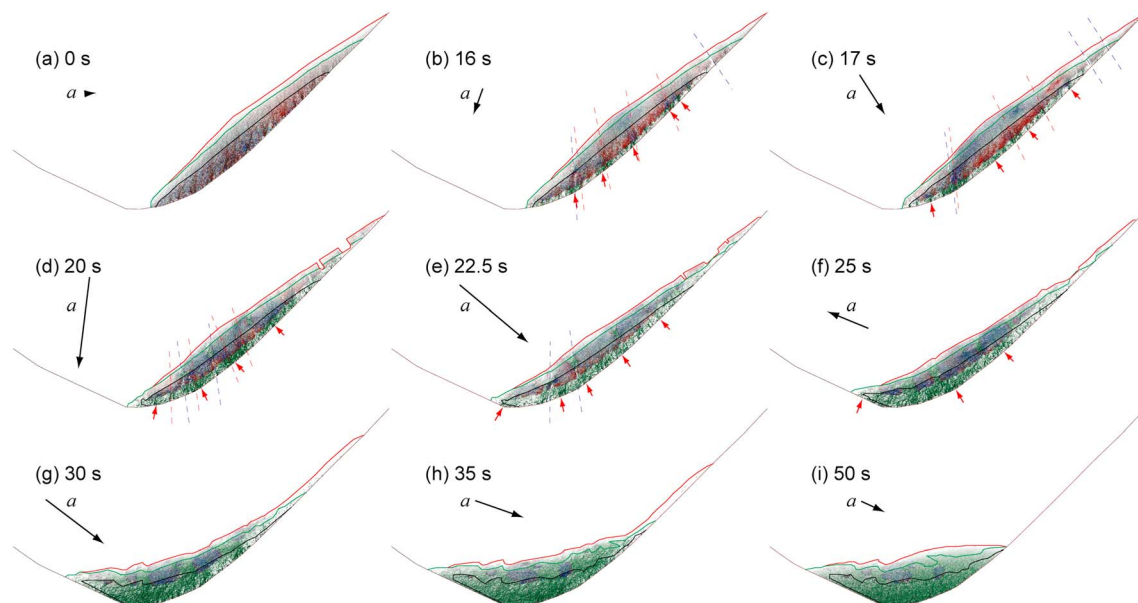

Figure 7. Distribution and evolution of force chains within the slope mass at time (a) 0 s, (b) 16 s, (c) 17s, (d) 20 s, (e) 22.5 s, (f) 25 s, (g) 30 s, (h) 35 s and (i) 50 s. The blue and red lines represent the normal compression and tension bonding forces; the black and green lines represent the normal and shear contact forces. The thickness of contact force chains is scaled down by a factor of 0.2, so that both bonding and contact force chains can be illustrated clearly on the same plot. Red dashed lines show the orientations of major force chains; blue dashed lines indicate the major cracks developed within the slope. The ground seismic acceleration is plotted as a vector on each figure. The scale of a is given in Figure 4a at the corresponding time.
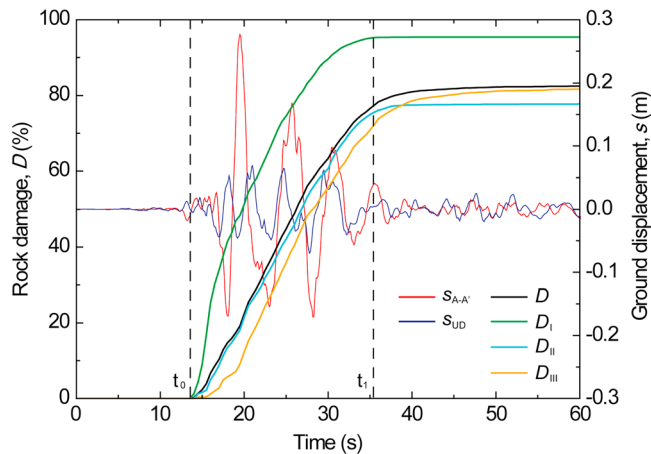
Figure 8. Evolution of rock damage in each slope layer and ground seismic shaking. $s_{A-A'}$ represents the ground horizontal displacement along the sliding direction, while s_{UD} represents the vertical displacement. D is the overall slope damage, while D_I, D_{II}, and D_{III} represent the rock damage in the slope layers I, II, and III, respectively.

cracks developed within the slope mass. According to the figure, it can be observed that before slope failure (Figure 7a), the force chains distribute loosely within the slope mass, and the force magnitude increases with depth due to gravitational compression. At relatively small ground shaking displacements, the major force chains are parallel to each other in a sub-vertical direction. These pillar-like strong force chains are surrounded by many weak force chains, forming a relatively stable slope structure. The distribution pattern of force chains can lead to strong internal resistance to landslide motion. As the ground shaking accelerates, intense shear stresses occur within the slope (see the green force chains), especially near the failure plane. The basal particle bonding forces disappear (i.e. bond breakage) when the seismic shaking-induced shear force exceeds the bonding strength. In addition, some preexisting weak force chains can also break due to intense shearing and ground seismic shaking-induced transient local dilation. Then, the shear stresses are shifted to the neighboring bonds. Thus, the thickness of force chains increases suddenly at several locations, as indicated by the red arrows on Figure 7b. In addition, the inclination angle of major force chains increases to almost perpendicular to the failure plane as the ground shaking proceeds (to the left, see the ground acceleration vector in Figure 7b), while it decreases as the ground moves backward (to the right, see Figure 7c). As the slope damage zone propagates gradually from the failure plane to the internal slope mass (see Figure 9), the whole slope mass is under a complete shearing state (see Figures 7g–7i).

The numerical result indicates that the pillar-like force chain structure is inherently sensitive to random directional forces (Hori et al., 2013). As stated in Johnson et al. (2016), the breakage of highly stressed force chains (at contacts) can cause a sudden drop of normal forces that generates elastic stress waves transmitting to the surrounding granular pack at a wavelength on the order of grain size. The wave energy is approximately close to the elastic energy initially stored at contacts. Then, the generated wave can be superposed with similar elastic waves, while traveling within the granular system. Thus, the highly energetic elastic wave can break more distant contacts and bonds into the slope mass. As more basal contacts and bonds continue to be broken up, the small cracks can nucleate and grow to completion quickly. According to Figure 7, after 17 s, a layer of interconnected shear contact force chains (i.e., the green lines) appears beneath the slope, showing that a completely fragmented debris layer has been developed. The fine fragments in this layer (e.g., fragmented and rounded particles) can significantly reduce the basal friction, increasing the overall mobility of the landslide. At 22.5 s, the detached slope mass collides onto the valley bottom and starts to move across a subcircular terrain at a high speed. Thus, high normal contact forces would concentrate at the slope toe region, together with the generation of high moment near the slope base. The high moment would lead to high tensile forces in the middle bottom region of the intact rock (see the red bonding force chains) and high compression forces at the middle slope surface. The localized high compressive and tensile forces at both locations can lead to the generation of new transversal cracks within the slope (see the blue dashed lines in Figures 7c–7e). The subsequent landslide propagation creates more internal damage, and the slope mass is gradually disintegrated into a large number of fine fragments. The final debris deposition is shown in plot Figure 7i with the major force chains being the normal and shear contact forces distributed vertically and parallelly to the slope inclination, respectively.

4.3. Evolution of Internal Slope Damage

A quantitative analysis of rock fragmentation during slope failure has been performed by plotting the evolution of internal rock damage ratio (D) over time in Figure 8. The rock damage ratio is defined as the percentage of broken bonds occurring during the landslide over the initial number of bonds in the intact slope mass. As stated by Zhao et al. (2017a), the evolution of D can effectively characterize the progressive damage of rock mass. In the analyses, the ground shaking displacements in the vertical (s_{UD}) and the sliding direction ($s_{A-A'}$) are also plotted in Figure 8 to illustrate the coseismic slope damage. According to Figure 8, it can be seen that the slope mass remains intact before 14 s (t_0) because of the very small intensity of seismic shaking. Between t_0 to t_1 (35.5 s), the ground shaking intensity increases abruptly, particularly in the sliding direction.
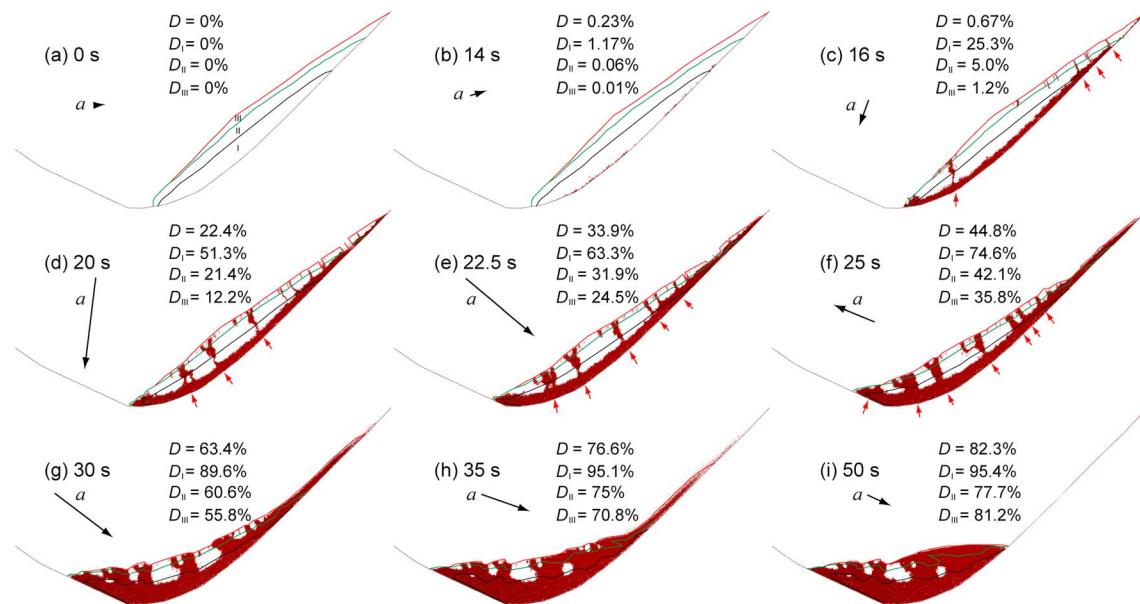
Figure 9. Distribution of accumulative slope damage during the landslide at time (a) 0 s, (b) 14 s, (c) 16 s, (d) 20 s, (e) 22.5 s, (f) 25 s, (g) 30 s, (h) 35 s and (i) 50 s. Red arrows indicate the major cracks and concentrated damage zones. The percentages of internal rock damage are also labeled on each plot. D is the overall slope damage, while D_I, D_{II}, and D_{III} represent the rock damage in the slope layers I, II, and III, respectively. The ground seismic acceleration (a) is plotted as a vector on each figure. The scale of a is given in Figure 4a at the corresponding time.

Thus, the percentage of slope damage increases very quickly with time, following approximately a linear relationship, until it reaches a relatively large value at t_1. The subsequent sliding and impacting of fragmented rock blocks onto the valley floor during the landslide deposition can lead to further increase of D. In this process, layer I suffers the highest damage among the three layers due to the intense shearing with the bedrock. Layer III also exhibits relatively high damage at the deposition stage, mainly because of its low strength and high compression loading near the ground surface. Layer II shows the smallest final rock damage, being constrained by the upper and bottom layers. The final stable peak values of D, D_I, D_{II}, and D_{III} are 82.6%, 95.4%, 77.8%, and 81.8%, respectively.

The distribution of accumulative slope damage can be visualized by plotting red dots within the slope profile at locations where interparticle bonds break, as illustrated in Figure 9. According to the figure, it is clear that at 14 s, the slope mass remains almost intact and only very few bond breakages occur near the failure plane. Then, as the ground shaking intensity increases, bond breakages accumulate gradually to form a connected fragmented granular layer beneath the slope mass (see Figure 9c), which facilitates the subsequent landslide propagation. In addition, several transversal cracks can be observed at the bottom and upper rear regions of the slope, as indicated by red arrows in Figure 9c. The locations of these major cracks are the same as those identified in Figure 7. The subsequent landslide propagation and deposition cause more damages to the slope mass, especially near the sliding front and rear regions, as reflected by the gradual enlargement of damage zones. The sliding front experiences intense interactions with the bedrock as the landslide collides onto the other bank of the valley, while the middle slope suffers strong compressions from the lower and upper slope regions. The upper rear region mainly contains some more superficial materials with a very weak rock structure prone to disintegration during motion. During the deposition stage in Figures 9g–9i, the transversal cracks grow to completion, together with the gradual increase of their thickness due to intense compression and shearing. In the middle region, the transversal damage zones also correspond to the slope decollement areas (see Figure 5). The final debris deposition in Figure 9i shows that the major part of the slope mass has been intensely fragmented and only several large rock blocks are wrapped by these fine fragments. The distribution pattern of large rock blocks in the final debris deposits can match well the field observations (Xu et al., 2009) that the middle layer contains many large boulders and blocks.

4.4. Reduction of Basal Stress Ratio

As stated by Campbell et al. (1995) and Johnson et al. (2016), some large and long runout landslides usually exhibit extremely low frictional resistance. The apparent landslide mobility can be effectively explained by
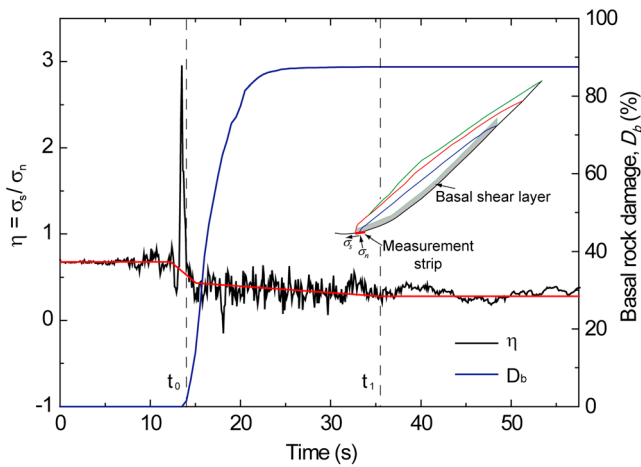
Figure 10. Variations of basal stress ratio and basal rock damage during landslide. The red line shows the general trend of basal stress ratio variation. The data points were obtained from the simulations at every 0.1 s.

the acoustic fluidization theory that the large and high-frequency pressure fluctuations generated during landsliding can relieve the overburden stresses (Melosh, 1979). Thus, it is necessary to analyze the variation of shear and normal stresses throughout the landslide motion. In this study, we defined a simple parameter of basal stress ratio (η) of shear (σ_s) to normal (σ_n) stresses as

$$\eta = \sigma_s/\sigma_n. \qquad (2)$$

In the analyses, σ_s and σ_n are measured at the base of slope toe (see the inset plot in Figure 10). The measured region is defined as a 30-m-long and 20-m-wide area, in which the total shear and normal forces acting on the basal bedrock are recorded during the simulation. Then, the corresponding stresses can be computed simply as the force divided by area. It should be noted that at static state, the definition of η only reflects how shear stress correlates with the normal stress, while at and after failure, η coincides with the definition of the coefficient of landslide friction (μ_0) according to the Coulomb's law of friction. In addition, the basal rock damage (D_b) is defined as the percentage of broken bonds to the initial total number of bonds for particles located at the slope basal layer with a thickness of around 25 m (i.e., the estimated thickness of basal shear zone; see the gray layer of the inset plot in Figure 10.). Here the definition of slope basal layer ignores the detached fragmented tail region because it has little influence on the variation of stresses at the landslide base.

Figure 10 illustrates the variation of η over time during the landslide simulation. According to the figure, it can be seen that from 0 to 12.5 s, η fluctuates slightly around a constant value of 0.68 due to seismic shaking. Then, it fluctuates abruptly from 0.31 to 2.95 during a short period of time near $t_0 = 14$ s before the slope failure. During the subsequent landslide propagation, the particle force chains form and break intermittently within the shear zone (see Figure 7), resulting in continuous fluctuation of basal stress ratio. The negative values of η occurring at 18 s are due to the change of shear stress direction as a result of sudden change of seismic shaking direction (see Figure 4b). It should be noted that before t_0, both the percentage of basal rock damage ($D_b = 0.1\%$) and slope deformation are negligibly small, which has little influence on η. Thus, the variation of η should only be attributed to the seismic shaking. Since the brittle rock mass cannot resist high tensile and shear stresses, the slope starts to break quickly after η reaches the peak value. After t_0, the failed slope mass accelerates to slide toward the valley bottom (see Figure 6), together with intense basal rock fragmentation. In this process, the fluctuation of η still exists but with tuned magnitudes, and D_b increases quickly to the peak value of 87.5% at 25 s.

The general trend of stress ratio variation (the red curve in Figure 10) indicates that during landslide motion (i.e., initiation, propagation, and deposition), the value of η (or μ_0) has been reduced significantly from 0.68 to 0.28. After $t_1 = 35.5$ s, η remains a relatively small value (≈ 0.28), because the debris mass has arrived at a stable deposition state and the initial pillar-like force chain network (see Figure 7) has been disintegrated completely. The obtained numerical results can match well the conclusions reached in De Blasio and Elverhøi (2008) that the effective friction at the base changes radically during sliding and the constant friction in Coulomb frictional law can no longer be used. In this process, the sliding occurs suddenly when the overburden stress is relieved by the variation of basal normal and shear stresses (or the apparent basal friction). As stated in Chialvo et al. (2012), during shear loading, the stress ratio of a granular assembly increases with the inertial number ($I = \dot{\gamma}d/\sqrt{p/\rho}$), following a relationship as below:

$$\eta(I) = \eta_s(\mu) + \frac{\alpha_1}{(I_0/I)^{\beta_1} + 1}, \qquad (3)$$

where $\eta_s(\mu)$ is the yield stress ratio determined by the interparticle friction coefficient; I_0, α_1, and β_1 are parameters governing the transition of granular rheology from quasi-static to inertial flow regime; $\dot{\gamma}$ is the shear rate; d is the particle diameter; and p is the confining pressure. The definition of inertial number shows the relative importance of shear deformation and particle rearrangement.
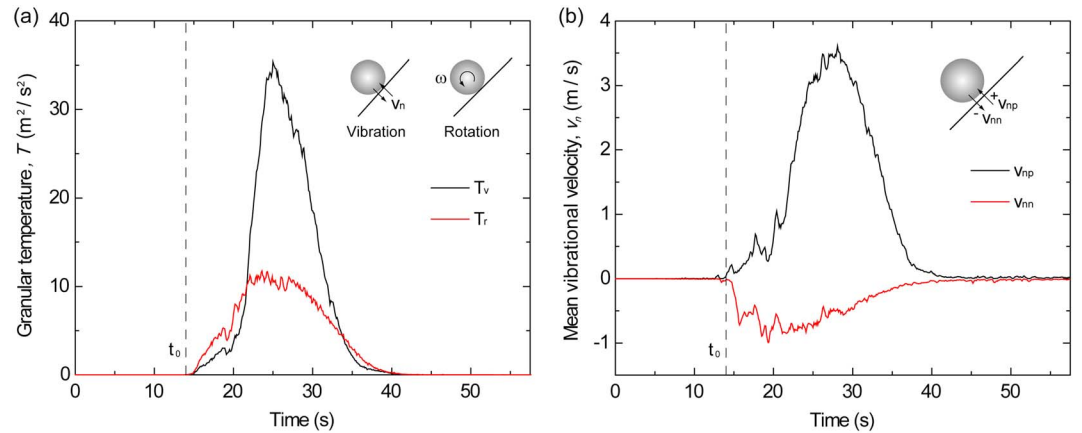
Figure 11. Evolution of (a) the vibrational (T_v) and rotational (T_r) granular temperatures and (b) the mean positive (v_{np}) and negative (v_{nn}) vibrational velocities normal to the slope.

The numerical results in our study show clearly that the basal stress ratio has been reduced significantly, which should be resulted from a corresponding decrease of granular inertial number. Thus, the effect of particle rearrangement should be dominant during landslide shearing. A possible explanation of particle rearrangement can be the combined effect of particle vibration and rotation within the basal slope shear zone. These two processes can lead to a highly agitated granular system (Campbell, 1989) and thus reduce the apparent landslide friction. In this study, the vibrational (T_v) and rotational (T_r) granular temperatures have been employed to quantify the intensity of particle agitation. Here the definition is given after Campbell (1990) as

$$T_v = \left\langle (v_n - \langle v_n \rangle)^2 \right\rangle, \tag{4}$$

$$T_r = \left\langle (\omega - \langle \omega \rangle)^2 \right\rangle, \tag{5}$$

where v_n is the translational velocity component normal to the failure plane and ω is the particle angular velocity (see the inset plot in Figure 11a). The angular bracket denotes the ensemble average over all particles located in the basal shear layer. As stated by Iverson (1997), the granular temperature represents a process of energy transformation from the particle translational to vibrational energy. The vibrational energy arises when the highly stressed particle contact and bonding force chains break, emitting elastic waves into the granular assembly at wavelengths on the order of particle size (Johnson et al., 2016). Consequently, the generated particle vibrations can effectively facilitate the rapid motion of landslide with increased mobility (Collins & Melosh, 2003). The particle rotation occurs due to continuous shear contacts in the basal fragmented layer.

Figure 11a illustrates the evolution of granular temperature for the basal shear layer of 25-m thickness. It can be seen that after slope failure (t_0), both rotational and vibrational granular temperatures increase immediately with time. There is a quick increase of both temperatures between 20 and 25 s due to landslide acceleration. T_v and T_r reach the peak values of 35.2 and 11.6 m^2/s^2, respectively, at around 25 s. Then, they both decrease gradually to nil when the bulk landslide mass ceases motion after 40 s. As stated by Campbell (1990), the dissipation of granular temperature is mainly due to interparticle collisions, and it can be very quick when external energy input (e.g., gravity work) stops. The evolution pattern of T_v and T_r indicates that a layer of agitated particles does exist at the slope base during landslide propagation, which can effectively reduce the landslide friction with increased mobility. Figure 11b illustrates the corresponding evolution of mean positive (v_{np}) and negative (v_{nn}) vibrational velocity components of particles with respect to the failure plane in the basal layer. Here the positive and negative velocities represent particle movements away from and toward the slope, respectively. It can be seen that both positive and negative particle velocities fluctuate slightly when the slope is close to fail. Then, both velocity components increase gradually with increased fluctuation intensities due to intense ground seismic shaking. v_{np} and v_{nn} reach the peak values of 3.6 and -0.99 m/s at 28 and 19.3 s, respectively. In this process, the high shearing stress together with the seismic
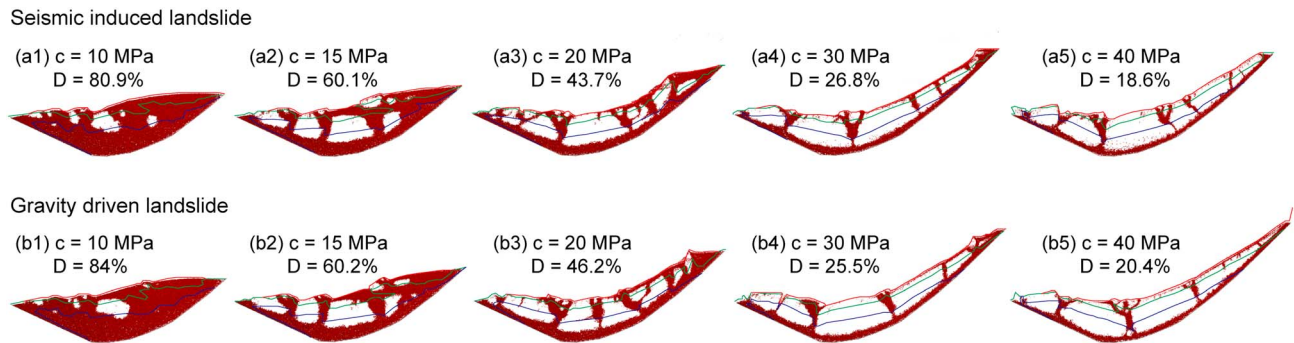
Figure 12. Distribution of slope internal damage in the final landslide deposits for tests with various particle bonding strengths. The plot series a1–a5 illustrate the results of seismic induced landslides, while b1–b5 illustrate the results of gravity driven landslides.

shaking at the base can break the pillar-like strong force chain networks, generating a layer of dispersed particles. The general trend shows that the magnitude of v_{np} is much larger than that of v_{nn}, meaning that during landslide propagation, particles in the basal shear layer tend to move away from the failure plane. This phenomenon illustrates clearly that during shearing, the initial closely packed, and interlocked particles would expand to create a dilative granular layer, reducing the overall particle interactions. As a result, the granular inertial number, slope shear strength, and bulk shear modulus will decrease significantly (Lambe & Whitman, 1969). Finally, the resulting vibration and rotation of particles will lead to a significant reduction of basal slope friction. The observed numerical results support well the hypothesis that vigorous agitation of grains exists at the base of the failing mass due to high shear rate, such that the landslide can spread with high mobility (Davies, 1982).

4.5. Influence of Particle Bonding Strength

As discussed in section 3, a set of rock properties has been employed in a preliminary numerical investigation of the coseismic Tangjiashan landslide. The obtained numerical results reveal the dynamic fragmentation and friction reduction of landslide during its propagation and deposition. To generalize this research, a systematic parametric study on the influence of bonding strength (c) on slope damage, basal stress ratio, landslide mobility, and granular temperature has also been performed. In testing the influence of bonding strength, the basal friction angle is fixed as 30°, while the bonding strength of particles in layer I (c_I) varies from 10 to 40 MPa. The reduced bonding strengths of $c_I/2$ and $c_I/3$ are assigned to particles in layers II and III, respectively, to consider the increased weathering intensity of upper slope layers. In addition, the same DEM model with unbonded slope base (i.e., the basal bonds between particles in layer I and the bedrock were deleted at the beginning of simulations) has been employed to simulate the slope failure driven by gravity force alone. In these tests, no seismic shaking was applied.

Figure 12 compares the distribution of final slope damage for tests on rock slopes with various strengths. It can be seen that for all tests the slope source stratigraphy can be well preserved and several large cracks and concentrated damage zones exist within the deposits. For the weak rock ($c = 10$ MPa), the slope mass was heavily fragmented ($D > 80\%$), particularly at the front and tail regions, such that the final deposition exhibits a relatively flat surface. The characteristics of complete slope fragmentation and a thick loose debris deposition layer at the tail of a weak rock slope can match some well-documented field observations (Chang & Zhang, 2010). For different tests, the percentage of overall rock damage decreases, while the deposit inclination angle increases with the particle bonding strength. For any specific particle bonding strength, the seismic-induced (Figures 12a1–12a5) and gravity-driven (Figures 12b1–12b5) landslides exhibit similar slope damage distribution pattern, indicating that fragmentation is an intrinsic property of landslide, irrespective of how it was triggered. The gravity-driven landslides experienced concentrated fragmentation at the slope base and middle portion, resulting in a thick fragmented basal layer and many transversal tension cracks (Figures 12b1–12b5). Thus, the overall slope damage in gravity-driven landslides is slightly larger than in seismic-induced landslides (Figures 12a1–12a5) because the slope mass suffers continuously strong basal shear stresses, while for seismic induced landslides, the shear stresses can be partly relieved by ground shaking. Figures 12a1 and 12a2 show a more intense fragmentation at the surface near the slope tail region than
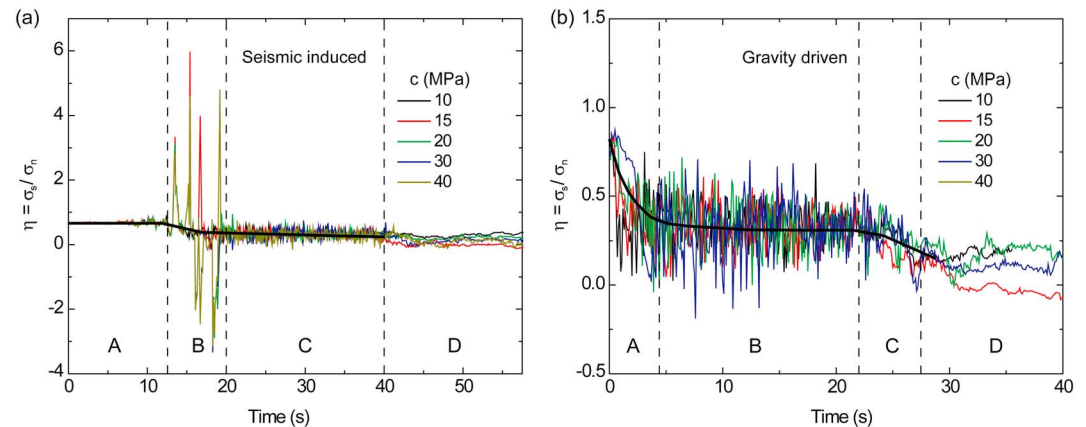
Figure 13. Evolution of basal stress ratio (η) for tests of various particle bonding strength (c). (a) The seismic induced landslides; (b) the gravity driven landslides. The general trend of basal stress ratio evolution is represented by thick black curves. The data points were obtained from the simulations at every 0.1 s.

the corresponding gravity driven cases. These damages near the tail surface result mainly from the initial seismic-induced tension cracks and subsequent collision of the detached tail blocks.

Figure 13 summarizes the evolution of basal stress ratio (η) for tests of various interparticle bonding strength and triggering mechanisms (i.e., Figure 13a seismic-induced and Figure 13b gravity-driven landslides). As shown in Figure 13a, the fluctuation pattern of η remains similar (as represented by the thick black curve) for all seismic-induced landslides, which can be classified into four stages (A–D). In stage A ($t < 12.5$ s), η remains almost constant because the seismic shaking intensity is still very low and the slope remains static. In stage B (12.5 s $\leq t < 20$ s), the seismic shaking intensity and slope damage increase quickly (see also Figures 4 and 8), leading η to fluctuate rapidly from the peak positive (approximately 6) to negative (approximately -3) values. The fluctuation of η becomes increasingly frequent for tests of high interparticle bonding strengths (e.g., $c = 40$ MPa). This is because the interaction between the strong slope mass and bedrock can be established and destroyed rapidly when the solid particles move coherently as a bonded block. The subsequent landslide deposition results in a gradual decrease of η for each test (see stage C). The final mean value of η is around 0.28 occurring after 40 s. In stage D, the bulk landslide deposit remains static except for some particles moving near the surface. Thus, η remains almost constant after $t = 40$ s. As a comparison, the gravity-driven landslides have a drastically different evolution pattern of basal stress ratio, as shown in Figure 13b. For these tests, η fluctuates rapidly about a mean (represented by a thick black curve), and the fluctuation intensity increases with the particle bonding strength. The general trend exhibits a similar four-stage pattern, but with reduced duration time. At the beginning of landslide propagation, η decreases sharply from the static stress ratio of 0.75 to 0.35 (stage A). Then, it remains almost constant for the subsequent landslide propagation and deposition phases (stage B). After $t = 22$ s, η decreases slowly as the bulk landslide mass gradually ceases motion (stage C). The landslide motion stops after $t = 27.5$ s, and η fluctuates slightly around a stable value (stage D). Figures 13a and 13b illustrate clearly that the reduction of basal stress ratio occurs mainly at the beginning of landslide propagation when the strong basal resistance, for example, bonding and static friction forces, is overcome by seismic- and gravity-induced shearing forces.

The numerical results are also analyzed with regard to the mobility of landslide mass in Figure 14a, where the apparent friction coefficient, H/L (H and L are the fall height and spreading length traveled by the center of a landslide mass, respectively), is plotted with respect to the particle bonding strength (c). It can be observed that despite of different triggering mechanisms employed in the two types of tests, H/L evolves similarly with c, following a parabolic relationship. The seismic-induced landslides have lower apparent friction coefficient than the gravity driven ones, especially for tests of $c \geq 30$ MPa, indicating that the seismic input energy can increase the landslide mobility to some extent. This result also shows that the peak value of H/L occurs at around $c = 30$ MPa, while relatively low values of H/L exist for tests of low ($c \leq 15$ MPa) and high ($c \geq 40$ MPa) particle bonding strengths. For these tests, H/L varies from 0.53 to 0.546, which can match some well-documented field observation data of long-runout landslides reported in Legros (2002) and Crosta et al. (2017). In addition, the overall slope damage ratio decreases exponentially with the particle bonding strength. The numerical results
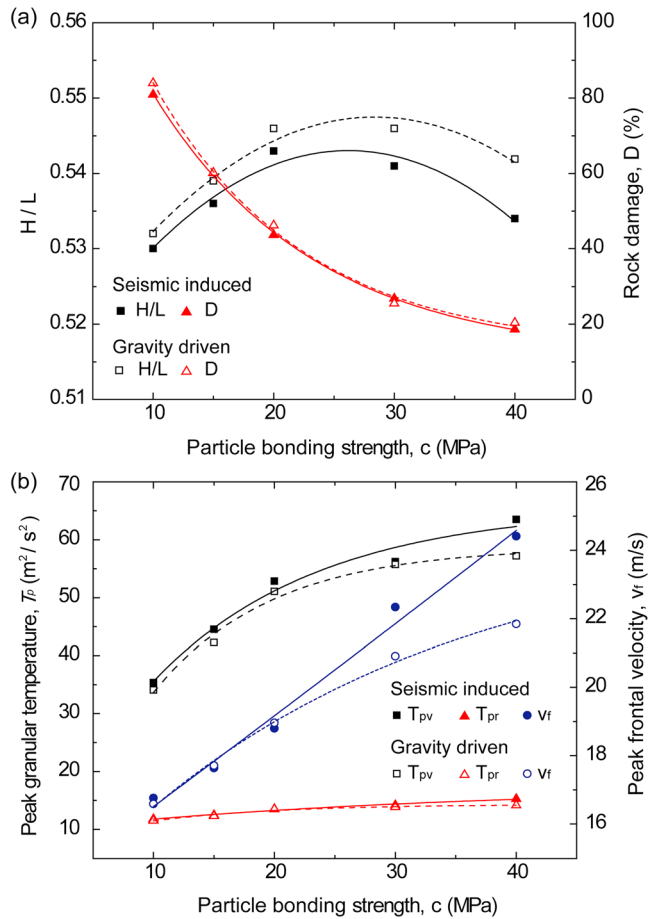
Figure 14. Variations of (a) apparent landslide friction coefficient (H/L) and slope rock damage ratio (D); (b) the peak vibrational (T_{pv}), rotational (T_{pr}) granular temperatures, and the landslide frontal velocity (v_f) with the particle bonding strength (c) for landslides induced by seismic shaking and gravity forces.

indicate that under the current testing conditions (i.e., seismic and gravity loading) and the slope volume, the strong rock slope can effectively resist seismic shaking and basal shear-induced fragmentation. This finding can match well the numerical observations in Zhao et al. (2018) on the dynamic fragmentation of intact and jointed rock blocks.

Figure 14b summarizes the variations of peak vibrational (T_{pv}), rotational (T_{pr}) granular temperatures, and landslide frontal propagation velocity (v_f) with the particle bonding strength for seismic-induced and gravity-driven landslides. It can be seen that in both types of tests, the peak granular temperatures and landslide frontal velocity, all increase with the particle bonding strength, following well exponential relationships. The peak vibrational temperatures (~35–60 m²/s²) are much higher than the peak rotational granular temperatures (~11–15 m²/s²), indicating that particle vibrations at the slope base play a major role in landslide motion. The decrease of slope damage ratio and increase of granular temperature with the particle bonding strength suggest that increasingly low energy dissipation and high basal granular agitation exist in the landslide basal shear layer. These conditions can effectively facilitate the increase of landslide mobility, as illustrated by the quick increase of peak landslide front propagation velocity in Figure 14b. In addition, v_f of the seismic-induced landslides becomes gradually larger than that of the gravity-driven ones, which is probably due to the low energy dissipation and extra energy input into the landslide mass by seismic shaking. According to Figure 14, the numerical results (i.e., D, T_{pv}, T_{pr}, and v_f) can be well fitted by exponential functions of the same form as

$$Y = A_1 e^{-c/t} + A_0, \tag{6}$$

where Y is the dependent variable (D, T_{pv}, T_{pr}, and v_f); A_0, A_1, and t are fitting constants; and c is the particle bonding strength.

5. Discussion

5.1. Dynamic Rock Fragmentation and Shear Resistance Reduction

The dynamic fragmentation of rock slope due to extremely high overloading stress would generate a layer of gradually fining and rounded solid particles at the base. These particles usually exhibit a much lower macroscopic shear strength than angular-shaped particles at a given confining pressure (Lambe & Whitman, 1969), which could effectively increase the landslide mobility (Perinotto et al., 2015). According to Figures 7 and 9, during landslide, the damage of rock mass concentrates mainly near the failure plane where the distribution of force chains is very loose. In particular, there is even some areas of negligibly small forces. As stated in Hori et al. (2013), this peculiar pattern of pillar-like strong force chains surrounded by weak force chains or noncontacted particles can form or break frequently within the granular mass during shearing. The breakage of these pillar-like strong force chains is accompanied by the release of elastic energy stored at contacts, resulting in a sudden drop of the granular friction coefficient (Dorostkar & Carmeliet, 2018; see also Figures 10 and 13 of this paper). The distribution patterns of force chains and rock damage indicate that the rock mass near the landslide base has been heavily fragmented by shearing (Zhang & McSaveney, 2017). As stated by Campbell (1989) and Cleary and Campbell (1993), for the case of a completely fragmented granular system, particles at the base are intensely agitated with frequent collisions and could act as a lubricating layer to reduce the overall effective friction of the granular flow. Under seismic loading, the energy input by seismic shaking can also increase the intensity of granular agitation. The intensity of particle agitation can be quantified by the vibrational and rotational granular temperatures in Figure 11a. In addition, the fracturing and fragmentation of rock also involve intense energy dissipations, together with boosts of granular momentum for some rock fragments, leading to the increase of landslide mobility (Crosta et al., 2017; De Blasio & Crosta, 2015; Zhao et al., 2017a).

According to Campbell et al. (1995), Strom (1999), and Chang and Taboada (2009), even though intense shearing exists within a completely fragmented slope, the landslide debris deposit exhibits approximately the same strata order as its original stratigraphic structure in the source mountainside after a long runout. This feature can also be well illustrated in the current study on the dynamic fragmentation of an initially intact rock slope (Figure 5). In addition, as shown in Figures 9d and 9e, the basal shear zone appears to have a uniform thickness along the basal surface. For a rough estimation, the thickness ranges from 20 to 27 m (~5–9 particle diameters). This value reflects how strongly the basal friction can influence the shear-induced dynamic slope fragmentation, which may effectively depend on the confining stress, shearing rate, rock strength, basal roughness, and slope volume. As stated in Campbell et al. (1995), high basal roughness can lead to the increase in thickness of landslide shear zone, reducing the final landslide runout. As the intact landslide mass moves atop the basal fragmented layer, it is straightforward to expect that the main source of energy dissipation comes from the shearing of basal granular layer (e.g., by friction and damping), while the intact rock block can remain elastic with very small energy dissipation (e.g., by damping during elastic deformation). If the frictional heat produced in the shear layer is high enough, it can even allow melting of the basal rocks, which could potentially lubricate the landslide motion (De Blasio & Elverhøi, 2008; Hu et al., 2018; Wang et al., 2017).

5.2. Slope Structure and Seismic Wave Reflection

This research aims to illustrate the initiation, propagation, and deposition mechanisms of seismic induced landslides by the discrete element modeling approach. Due to the high computational cost for the real 3-D DEM modeling, only a 2-D plane strain model has been employed. The presented results reveal that the failure of a complex coseismic landslide can be reproduced, at least in a reasonably qualitative way, by the DEM model. Relatively large particles were used in this study to represent the slope mass, as a compromise of computational cost. It should also be noted that the confining pressure, brittle deformation, initial weathering condition, joints, and fractures were not considered because they are not within the purview of this study.

The current research has not considered the influence of seismic shaking amplification due to ground topography. For simplicity and convenience of DEM model configuration, the current study simply employed the same seismic wave excitations along a horizontal bedrock layer. This approach may lead to slightly different loading conditions on the layered slope structure and cause some minor errors to the computation of slope displacement. In fact, the seismic shaking can be amplified at the slope surface due to wave reflection and diffraction by ground topography irregularities (Jafarzadeh et al., 2015). As a result, additional seismic loading forces can be imposed on the landslide mass. Correct evaluation of this amplification effect is complicated because detailed analyses of slope topography, soil properties, frequency, and angle of incident seismic wave are required. In addition, the errors resulting from the seismic wave attenuation along the traveling path (e.g., the Qingping Station is 46 km away from the studied site) can be much larger than that from shaking amplification. Thus, for qualitative analyses, the accuracy of current study is believed to be acceptable. During DEM simulations, the rigid basal boundary condition along the failure plane may reflect the long wavelength seismic waves into the slope, which in turn erroneously amplifies the seismic loading (McNamara, 2013). For this problem, a layer of soft particles fixed on the rigid boundary in this study can effectively represent an absorbing boundary condition, in which the energy of reflected waves can be absorbed via an artificially high damping. Furthermore, as stated in Johnson et al. (2016), the long wavelength acoustic waves have little influence on the overall debris dynamics, as only the short wavelength acoustic waves are of primary importance. These short acoustic waves control the potential reduction of effective friction for the rockslide and can be effectively determined by the constituent particle sizes. Therefore, the basal boundary of fixed fine particles with high damping coefficient employed in the current numerical simulations is believed to be reasonable for analyzing earthquake-induced landslides.

6. Conclusions

This paper presents an efficient numerical technique for analyzing the dynamic fragmentation and lubrication mechanisms of coseismic landslides via 2-D plane strain DEM simulations. The slope profile is represented by smooth and rigid walls, while the layered structure of slope mass is reproduced by packing an

assembly of bonded spherical particles with various microscopic properties. By employing this DEM model together with recorded seismic waves, the failure and dynamics of Tangjiashan landslide have been analyzed.

The landslide is initiated when the input seismic motion reaches the peak value and the shear forces are dominant at the base. In the meantime, the slope overburden stress is relieved, and the basal stress ratio decreases rapidly. After failure, the basal slope mass is fragmented progressively as intense shearing continues, which in turn facilitates the acceleration of landslide propagation. The basal shear layer has a thickness of 5–9 particle diameters. In this process, the basal stress ratio decreases gradually from 0.68 to 0.28 by granular agitation from a combined effect of particle vibration and rotation. The corresponding vibrational and rotational granular temperatures first increase quickly to the peak values of 35.2 and 11.6 m^2/s^2, respectively, due to intense basal shearing, and then decrease gradually to nil when the solid materials cease motion. The reduction of basal stress ratio occurs when the strong basal resistance is overcome by seismic- and gravity-induced shear forces, and the particle rearrangements become dominant within the basal shear layer. During emplacement, the slope source stratigraphic relations are preserved apart from the frontal region where a reversal is partially observed. The collision of the detached slope with the valley floor and compression between rock blocks lead to concentrated contact force chains and severe slope damages. The overall rock damage ratio decreases, while the peak vibrational and rotational temperatures, landslide frontal propagation velocity increase with the particle bonding strength, following exponential relationships. The seismic-induced and gravity-driven landslides exhibit similar evolution patterns of slope damage, suggesting that the dynamic fragmentation is an intrinsic feature of landslide material irrespective of the triggering mechanism.

This research shows that the seismic shaking appears to be more relevant to the detachment than to the spreading of the landslide mass. The reduction of rock block size by widespread fracture propagation and rock fragmentation is a prerequisite condition for landslide mobilization. Further research on landslide mobilization should consider the detailed fracture or joint distributions within the initial slope mass, as these aspects can also dominate the fragmentation and lubrication mechanisms of landslides.

References

Abe, S., Place, D., & Mora, P. (2004). A parallel implementation of the lattice solid model for the simulation of rock mechanics and earthquake dynamics. *Pure and Applied Geophysics*, *161*(11–12), 2265–2277. https://doi.org/10.1007/s00024-004-2562-x

Bowman, E. T., & Take, W. A. (2015). The runout of chalk cliff collapses in England and France—Case studies and physical model experiments. *Landslides*, *12*(2), 225–239. https://doi.org/10.1007/s10346-014-0472-2

Bowman, E. T., Take, W. A., Rait, K. L., & Hann, C. (2012). Physical models of rock avalanche spreading behaviour with dynamic fragmentation. *Canadian Geotechnical Journal*, *49*(4), 460–476. https://doi.org/10.1139/t2012-007

Campbell, C. S. (1989). Self-lubrication for long runout landslides. *The Journal of Geology*, *97*(6), 653–665. https://doi.org/10.1086/629350

Campbell, C. S. (1990). Rapid granular flows. *Annual Review of Fluid Mechanics*, *22*(1), 57–90. https://doi.org/10.1146/annurev.fl.22.010190.000421

Campbell, C. S., Cleary, P. W., & Hopkins, M. (1995). Large-scale landslide simulations: Global deformation, velocities and basal friction. *Journal of Geophysical Research*, *100*(B5), 8267–8283. https://doi.org/10.1029/94JB00937

Cascini, L., Cuomo, S., Pastor, M., Sorbino, G., & Piciullo, L. (2014). SPH run-out modelling of channelised landslides of the flow type. *Geomorphology*, *214*, 502–513. https://doi.org/10.1016/j.geomorph.2014.02.031

Chang, D. S., & Zhang, L. M. (2010). Simulation of the erosion process of landslide dams due to overtopping considering variations in soil erodibility along depth. *Natural Hazards and Earth System Sciences*, *10*(4), 933–946. https://doi.org/10.5194/nhess-10-933-2010

Chang, K. J., & Taboada, A. (2009). Discrete element simulation of the Jiufengershan rock-and-soil avalanche triggered by the 1999 Chi-Chi earthquake, Taiwan. *Journal of Geophysical Research*, *114*, F03003. https://doi.org/10.1029/2008JF001075

Chialvo, S., Sun, J., & Sundaresan, S. (2012). Bridging the rheology of granular flows in three regimes. *Physical Review E*, *85*(2), 021305. https://doi.org/10.1103/PhysRevE.85.021305

Chigira, M., Wu, X., Inokuchi, T., & Wang, G. (2010). Landslides induced by the 2008 Wenchuan earthquake, Sichuan, China. *Geomorphology*, *118*(3–4), 225–238. https://doi.org/10.1016/j.geomorph.2010.01.003

Cleary, P. W., & Campbell, C. S. (1993). Self-lubrication for long runout landslides: Examination by computer simulation. *Journal of Geophysical Research*, *98*(B12), 21,911–21,924. https://doi.org/10.1029/93JB02380

Collins, G. S., & Melosh, H. J. (2003). Acoustic fluidization and the extraordinary mobility of sturzstroms. *Journal of Geophysical Research*, *108*(B10), 2473. https://doi.org/10.1029/2003JB002465

Crosta, G. B., De Blasio, F. V., De Caro, M., Volpi, G., Imposimato, S., & Roddeman, D. (2017). Modes of propagation and deposition of granular flows onto an erodible substrate: Experimental, analytical, and numerical study. *Landslides*, *14*(1), 47–68. https://doi.org/10.1007/s10346-016-0697-3

Crosta, G. B., Frattini, P., Fusi, N., & Sosio, R. (2011). Formation, characterisation and modeling of the Val Pola rock-avalanche dam (Italy). In *Natural and artificial rockslide dams*, (pp. 347–368). Berlin Heidelberg: Springer.

Cundall, P. A., & Strack, O. D. L. (1979). A discrete numerical model for granular assemblies. *Geotechnique*, *29*(1), 47–65.

Dai, F. C., Xu, C., Yao, X., Xu, L., Tu, X. B., & Gong, Q. M. (2011). Spatial distribution of landslides triggered by the 2008 Ms 8.0 Wenchuan earthquake, China. *Journal of Asian Earth Sciences*, *40*(4), 883–895. https://doi.org/10.1016/j.jseaes.2010.04.010

Davies, T. H. (1982). Spreading of rock avalanche debris by mechanical fluidization. *Rock Mechanics*, *15*(1), 9–24. https://doi.org/10.1007/bf01239474

De Blasio, F., & Crosta, G. B. (2015). Fragmentation and boosting of rock falls and rock avalanches. *Geophysical Research Letters*, *42*, 8463–8470. https://doi.org/10.1002/2015GL064723

De Blasio, F. V., & Elverhøi, A. (2008). A model for frictional melt production beneath large rock avalanches. *Journal of Geophysical Research*, *113*, F02014. https://doi.org/10.1029/2007JF000867

Dorostkar, O., & Carmeliet, J. (2018). Potential energy as metric for understanding stick–slip dynamics in sheared granular fault gouge: A coupled CFD–DEM study. *Rock Mechanics and Rock Engineering*, *51*(10), 3281–3294. https://doi.org/10.1007/s00603-018-1457-6

Evans, S. G., Hermanns, R. L., & Strom, A. (2011). *Natural and artificial rockslide dams*, (Vol. 133). Verlag Berlin Heidelberg: Springer. https://doi.org/10.1007/978-3-642-04764-0

Evans, S. G., Tutubalina, O. V., Drobyshev, V. N., Chernomorets, S. S., McDougall, S., Petrakov, D. A., & Hungr, O. (2009). Catastrophic detachment and high-velocity long-runout flow of Kolka Glacier, Caucasus Mountains, Russia in 2002. *Geomorphology*, *105*(3–4), 314–321. https://doi.org/10.1016/j.geomorph.2008.10.008

Fan, X., van Westen, C. J., Xu, Q., Gorum, T., & Dai, F. (2012). Analysis of landslide dams induced by the 2008 Wenchuan earthquake. *Journal of Asian Earth Sciences*, *57*(0), 25–37. https://doi.org/10.1016/j.jseaes.2012.06.002

Fukuoka, H., Wang, G., Sassa, K., Wang, F., & Matsumoto, T. (2004). Earthquake-induced rapid long-traveling flow phenomenon: May 2003 Tsukidate landslide in Japan. *Landslides*, *1*(2), 151–155. https://doi.org/10.1007/s10346-004-0019-z

Goodman, R. E. (1989). *Introduction to rock mechanics*, (2nd ed.). New York: John Wiley & Sons.

Gorum, T., Fan, X., van Westen, C. J., Huang, R. Q., Xu, Q., Tang, C., & Wang, G. (2011). Distribution pattern of earthquake-induced landslides triggered by the 12 May 2008 Wenchuan earthquake. *Geomorphology*, *133*(3–4), 152–167. https://doi.org/10.1016/j.geomorph.2010.12.030

Hoek, E., & Brown, E. T. (1997). Practical estimates of rock mass strength. *International Journal of Rock Mechanics and Mining Sciences*, *34*(8), 1165–1186. https://doi.org/10.1016/S1365-1609(97)80069-X

Hori, T., Sakaguchi, H., Yoshioka, N., & Kaneda, Y. (2013). Shear resistance reduction due to vibration in simulated fault gouge. In *Earthquakes: Radiated energy and the physics of faulting*, (pp. 135–142). Washington, DC: American Geophysical Union.

Hu, W., Huang, R. Q., McSaveney, M., Zhang, X. H., Yao, L., & Shimamoto, T. (2018). Mineral changes quantify frictional heating during a large low-friction landslide. *Geology*, *46*(3), 223–226. https://doi.org/10.1130/G39662.1

Huang, C. C., & Yuin, S. C. (2010). Experimental investigation of rainfall criteria for shallow slope failures. *Geomorphology*, *120*(3–4), 326–338. https://doi.org/10.1016/j.geomorph.2010.04.006

Huang, R., & Fan, X. (2013). The landslide story. *Nature Geoscience*, *6*(5), 325–326. https://doi.org/10.1038/ngeo1806.

Huang, R., Pei, X., Fan, X., Zhang, W., Li, S., & Li, B. (2012). The characteristics and failure mechanism of the largest landslide triggered by the Wenchuan earthquake, May 12, 2008, China. *Landslides*, *9*(1), 131–142. https://doi.org/10.1007/s10346-011-0276-6

Huang, R. Q., & Li, W. L. (2009). Analysis of the geo-hazards triggered by the 12 May 2008 Wenchuan earthquake, China. *Bulletin of Engineering Geology and the Environment*, *68*(3), 363–371. https://doi.org/10.1007/s10064-009-0207-0

Iverson, R. M. (1997). The physics of debris flows. *Reviews of Geophysics*, *35*(3), 245–296. https://doi.org/10.1029/97RG00426

Jafarzadeh, F., Shahrabi, M. M., & Farahi Jahromi, H. (2015). On the role of topographic amplification in seismic slope instabilities. *Journal of Rock Mechanics and Geotechnical Engineering*, *7*(2), 163–170. https://doi.org/10.1016/j.jrmge.2015.02.009

Jiang, M. J., Jiang, T., Crosta, G. B., Shi, Z. M., Chen, H., & Zhang, N. (2015). Modeling failure of jointed rock slope with two main joint sets using a novel DEM bond contact model. *Engineering Geology*, *193*, 79–96. https://doi.org/10.1016/j.enggeo.2015.04.013

Jibson, R., & Harp, E. (2016). Ground motions at the outermost limits of seismically triggered landslides. *Bulletin of the Seismological Society of America*, *106*(2), 708–719. https://doi.org/10.1785/0120150141

Jing, L., Kwok, C. Y., Leung, Y. F., & Sobral, Y. D. (2016). Characterization of base roughness for granular chute flows. *Physical Review E*, *94*(5), 052901.

Johnson, B. C., & Campbell, C. S. (2017). Drop height and volume control the mobility of long-runout landslides on the earth and Mars. *Geophysical Research Letters*, *44*, 12,091–12,097. https://doi.org/10.1002/2017GL076113

Johnson, B. C., Campbell, C. S., & Melosh, H. J. (2016). The reduction of friction in long runout landslides as an emergent phenomenon. *Journal of Geophysical Research: Earth Surface*, *121*, 881–889. https://doi.org/10.1002/2015JF003751

Katz, O., Morgan, J. K., Aharonov, E., & Dugan, B. (2014). Controls on the size and geometry of landslides: Insights from discrete element numerical simulations. *Geomorphology*, *220*, 104–113. https://doi.org/10.1016/j.geomorph.2014.05.021

Khazai, B., & Sitar, N. (2004). Evaluation of factors controlling earthquake-induced landslides caused by Chi-Chi earthquake and comparison with the Northridge and Loma Prieta events. *Engineering Geology*, *71*(1–2), 79–95. https://doi.org/10.1016/S0013-7952(03)00127-3

Kokusho, T., & Ishizawa, T. (2007). Energy approach to earthquake-induced slope failures and its implications. *Journal of Geotechnical and Geoenvironmental Engineering*, *133*(7), 828–840. https://doi.org/10.1061/(ASCE)1090-0241(2007)133:7(828)

Lambe, T. W., & Whitman, R. V. (1969). *Soil mechanics*. New York: John Wiley and Sons.

Legros, F. (2002). The mobility of long-runout landslides. *Engineering Geology*, *63*(3–4), 301–331. https://doi.org/10.1016/S0013-7952(01)00090-4

Li, Z., Xu, Y., Huang, R., Hao, T., Xu, Y., Liu, J., & Liu, J. (2011). Crustal P-wave velocity structure of the Longmenshan region and its tectonic implications for the 2008 Wenchuan earthquake. *Science China Earth Sciences*, *54*(9), 1386. https://doi.org/10.1007/s11430-011-4177-2–1393

McNamara, S. (2013). Absorbing boundary conditions for granular acoustics. Paper Presented at the III International Conference on Particle Based Methods—Fundamentals and Application, PARTICLES 2013, Stuttgart, Germany.

Melosh, H. J. (1979). Acoustic fluidization: A new geologic process? *Journal of Geophysical Research*, *84*(B13), 7513–7520. https://doi.org/10.1029/JB084iB13p07513

Meunier, P., Hovius, N., & Haines, A. J. (2007). Regional patterns of earthquake-triggered landslides and their relation to ground motion. *Geophysical Research Letters*, *34*, L20408. https://doi.org/10.1029/2007GL031337

Palmer, J. (2017). Creeping earth could hold secret to deadly landslides. *Nature*, *548*(7668), 384–386. https://doi.org/10.1038/548384a

Perinotto, H., Schneider, J. L., Bachèlery, P., Le Bourdonnec, F. X., Famin, V., & Michon, L. (2015). The extreme mobility of debris avalanches: A new model of transport mechanism. *Journal of Geophysical Research: Solid Earth*, *120*, 8110–8119. https://doi.org/10.1002/2015JB011994

Potyondy, D. O., & Cundall, P. A. (2004). A bonded-particle model for rock. *International Journal of Rock Mechanics and Mining Sciences*, *41*(8), 1329–1364. https://doi.org/10.1016/j.ijrmms.2004.09.011

Seismosoft (2017). Seismosoft: Earthquake engineering software solutions. *SeismoSignal*. From http://www.seismosoft.com/seismosignal

Strom, A. L. (1999). The morphology and internal structure of large rockslides as indicators of their formational mechanisms. *Doklady Earth Sciences*, *369*(8), 1079–1081.

Tang, C., Zhu, J., Qi, X., & Ding, J. (2011). Landslides induced by the Wenchuan earthquake and the subsequent strong rainfall event: A case study in the Beichuan area of China. *Engineering Geology*, *122*(1–2), 22–33. https://doi.org/10.1016/j.enggeo.2011.03.013

Utili, S., Zhao, T., & Houlsby, G. T. (2015). 3D DEM investigation of granular column collapse: Evaluation of debris motion and its destructive power. *Engineering Geology*, *186*(0), 3–16. https://doi.org/10.1016/j.enggeo.2014.08.018

Wang, Y. F., Dong, J. J., & Cheng, Q. G. (2017). Velocity-dependent frictional weakening of large rock avalanche basal facies: Implications for rock avalanche hypermobility? *Journal of Geophysical Research: Solid Earth*, *122*, 1648–1676. https://doi.org/10.1002/2016JB013624

Wu, C. H., Chen, S. C., & Feng, Z. Y. (2014). Formation, failure, and consequences of the Xiaolin landslide dam, triggered by extreme rainfall from Typhoon Morakot, Taiwan. *Landslides*, *11*(3), 357–367. https://doi.org/10.1007/s10346-013-0394-4

Wu, J. P., Huang, Y., Zhang, T. Z., Ming, Y. H., & Fang, L. H. (2009). Aftershock distribution of the MS8.0 Wenchuan earthquake and 3-D P-wave velocity structure in and around source region. *Chinese Journal of Geophysics*, *52*(1), 102–111. https://doi.org/10.1002/cjg2.1331

Xu, Q., Fan, X. M., Huang, R. Q., & Westen, C. (2009). Landslide dams triggered by the Wenchuan earthquake, Sichuan Province, south West China. *Bulletin of Engineering Geology and the Environment*, *68*(3), 373–386. https://doi.org/10.1007/s10064-009-0214-1

Xu, W. J., Xu, Q., & Wang, Y. J. (2013). The mechanism of high-speed motion and damming of the Tangjiashan landslide. *Engineering Geology*, *157*(0), 8–20. https://doi.org/10.1016/j.enggeo.2013.01.020

Yin, Y., Wang, F., & Sun, P. (2009). Landslide hazards triggered by the 2008 Wenchuan earthquake, Sichuan, China. *Landslides*, *6*(2), 139–152. https://doi.org/10.1007/s10346-009-0148-5

Zhang, M., & McSaveney, M. J. (2017). Rock avalanche deposits store quantitative evidence on internal shear during runout. *Geophysical Research Letters*, *44*, 8814–8821. https://doi.org/10.1002/2017GL073774

Zhao, T., Crosta, G. B., Utili, S., & De Blasio, F. V. (2017a). Investigation of rock fragmentation during rockfalls and rock avalanches via 3-D discrete element analyses. *Journal of Geophysical Research: Earth Surface*, *122*, 678–695. https://doi.org/10.1002/2016JF004060

Zhao, T., Crosta Giovanni, B., Dattola, G., & Utili, S. (2018). Dynamic fragmentation of jointed rock blocks during rockslide-avalanches: Insights from discrete element analyses. *Journal of Geophysical Research: Solid Earth*, *123*, 3250–3269. https://doi.org/10.1002/2017JB015210

Zhao, T., Dai, F., & Xu, N. W. (2017b). Coupled DEM-CFD investigation on the formation of landslide dams in narrow rivers. *Landslides*, *14*(1), 189–201. https://doi.org/10.1007/s10346-015-0675-1

Zhao, T., Dai, F., Xu, N. W., Liu, Y., & Xu, Y. (2015). A composite particle model for non-spherical particles in DEM simulations. *Granular Matter*, *17*(6), 763–774. https://doi.org/10.1007/s10035-015-0596-7

Zhao, T., Utili, S., & Crosta, G. B. (2016). Rockslide and impulse wave modelling in the Vajont reservoir by DEM-CFD analyses. *Rock Mechanics and Rock Engineering*, *49*(6), 2437–2456. https://doi.org/10.1007/s00603-015-0731-0